Supplement of Atmos. Chem. Phys., 26, 12211–12229, 2026
https://doi.org/10.5194/acp-26-12211-2026-supplement

Atmospheric Chemistry and Physics
Open Access
EGU

Supplement of

Sea surface warming suppresses primary sea spray aerosol number production

Raymond J. Leibensperger III et al.

Correspondence to: Kimberly A. Prather (kprather@ucsd.edu)

S1 Previous Literature

The dependence of sea spray aerosol (SSA) production on sea surface temperature (SST) has long been investigated in the laboratory and field. To target specific processes and elements of this complicated relationship, laboratory studies have used a variety of wave breaking analogues, complicating the comparisons of findings. A summary of previous studies is included in Table S1. Of the 18 previous studies encompassing 24 independent SSA-SST relationships, eight identified a positive dependence, nine identified a negative dependence, and seven identified a non-monotonic dependence. Here, we provide brief summaries of each study as it relates to our results, but we refer the reader to each study for in depth information. Laboratory studies are described first followed by field studies, each described in chronological order.

Laboratory studies offer a controlled approach to elucidating SSA-SST dependencies, with the quality of wave breaking analogues constantly improving. Mårtensson et al. (2003) utilized a sintered glass filter to generate SSA from synthetic sea salt and reported size-dependent results: for $D_p > 0.35$ μm number concentrations increased by ten times and for $D_p < 0.07$ μm they decreased by three times over the SST range of -2 to 25 °C. Nearly a decade later, Zábori et al. (2012) observed that SSA number concentrations generated by a plunging jet decreased over SSTs from -1 to 9 °C using Arctic Ocean water. The same trend was observed by Salter et al. (2014) using artificial seawater, but at 10 °C SSA number concentrations stabilized and remained constant up to 30 °C. They also found a similar trend for surface bubble concentrations with a film radius greater than 0.25 mm. Again using artificial seawater and a plunging jet, Salter et al. (2015) found a similar negative dependence of submicron SSA on SST. However, the opposite was true for supermicron SSA: concentrations increased with increasing SST from -1 to 30 °C.

The discrepancies observed when differing wave breaking analogues and water types are used led Forestieri et al. (2018) to utilize a Marine Aerosol Reference Tank (MART) and mini-MART with water types ranging from NaCl to filtered seawater. Using seawater sourced from the same location as used in this study and the mini-MART, Forestieri et al. found no clear relationship between SSA concentrations and SST. However, MART and mini-MART experiments showed an increase of accumulation mode SSA with increasing SSTs using NaCl and reef salt. Christiansen et al. (2019) compared results from a diffuser and plunging jet using artificial seawater across a -2 to 35 °C temperature range. From -2 to 10 °C, results from the plunging jet aligned with Zábori et al. (2012), Salter et al. (2014), and Salter et al. (2015), but concentrations increased above 10 °C. Single bubble experiments by Nielsen and Bilde (2020) showed that particle concentrations were orders of magnitude lower at 19 °C compared to 0 °C.

More recently, using Mediterranean seawater, Sofieva et al. (2022) reported similar results as earlier diffuser experiments over a 2 to 30 °C temperature range. Zinke et al. (2022) showed that SSA production flux from artificial seawater decreases from 0

to ~15 °C and increases from 20 to 30 °C. Similarly, but across various natural water types, Sellegri et al. (2023) reported a similar trend for production flux. However, they did not observe a slight increase as Zinke et al. above 15 °C. Finally, Hu et al. (2024) compared results from a plunging jet and plunging waterfall over 0 to 30 °C in natural seawater. Like Christiansen et al. and Forestieri et al., the alternative wave breaking analogue produced different results. The combination of these studies highlights the importance of representative SSA production and how subtle differences in seawater composition can significantly alter the end results.

In addition to these laboratory studies, several recent studies use field observations to characterize the role of SST in determining SSA production. The study of Jaeglé et al. (2011) combines shipborne and station-based observations of SSA mass concentrations with satellite-retrieved and station-based aerosol optical depth estimations and simulations in the GEOS-Chem model, finding a third-order polynomial function of SST best fits the increasing mass concentration measurements with increasing SSTs. In another study with global coverage, Grythe et al. (2014) use ship- and station-based SSA mass concentrations coupled with FLEXPART simulations to determine a positive, linear trend in mass concentrations with increasing SSTs, but note a variety of relationships occur with several exhibiting a negative relationship.

A North Atlantic cruise focusing on environmental conditions across three eddies found that their ship-based accumulation mode SSA number concentration measurements scaled negatively with increasing SSTs, with SSTs being the strongest correlated environmental parameter in the case study ($R \sim 0.8$) (Lehahn et al., 2014). Another North Atlantic ship-based study used measurements of number fluxes with station-based number concentration measurements and model-based wave parameters to develop a new SSA source function with a monotonic, positive relationship between number fluxes and SSTs (Ovadnevaite et al., 2014). Yet another North Atlantic cruise used shipborne number concentration measurements to determine a weak negative relationship between number concentration and SSTs ($R = -0.2$) but a positive correlation between mass concentrations and SSTs ($R = 0.3$) across all measurements (Saliba et al., 2019). Interestingly, these correlations become strong with the study median values, where total SSA number concentrations exhibit a correlation value of -0.67 while total SSA mass concentrations have a correlation value of 0.76 with increasing SSTs.

Liu et al. (2021) found a positive relationship ($R = 0.46$) between airborne volume concentration measurements from the Atmospheric Tomography Mission (AToM) and SSTs, after removing the effect of wind speed. Lastly, a recent study used observations of number and volume fluxes from 18 cruises across the North Atlantic Ocean and Baltic Sea to characterize a statistically significant negative correlation between number fluxes and SSTs ($R < -0.5$, $p < 10^{-12}$) and a weaker but significant positive correlation between volume fluxes and SSTs ($R \sim 0.4$, $p < 0.05$), with the exact correlation strengths depending on biological activity (Markuszewski et al., 2024).

	Reference	Study Type	Analog or Ocean Basin	Measurement Type	SSA-SST Dependence
1	Mårtensson et al. (2003)	Laboratory	Sintered Glass Filter	Size-resolved SSA number and subsurface bubble concentrations	Number Concentrations: Non-monotonic
2	Zábori et al. (2012)	Laboratory	Plunging Jet	Size-resolved SSA number concentrations	Number Concentrations: Non-monotonic
3	Salter et al. (2014)	Laboratory	Plunging Jet	Size-resolved SSA number and subsurface bubble concentrations, air entrainment	Number Concentrations: Negative
4	Salter et al. (2015)	Laboratory	Plunging Jet	Size-resolved SSA number concentrations and flux	Number Concentrations: Negative (submicron), Positive (supermicron) Number Fluxes: Negative (submicron), Positive (supermicron)
5	Forestieri et al. (2018)	Laboratory	miniMART	Size-resolved SSA number concentrations	Number Concentrations: Positive
6	Christiansen et al. (2019)	Laboratory	Plunging Jet Diffuser	Size-resolved SSA number concentrations, air entrainment	Jet Number Concentrations: Non-monotonic Diffuser Number Concentrations: Negative
7	Nielsen & Bilde (2020)	Laboratory	Pipette Bubbler	SSA number concentrations	Number Concentrations: Negative
8	Sofieva et al. (2022)	Laboratory	Diffuser	Size-resolved SSA number concentrations	Number Concentrations: Non-monotonic
9	Zinke et al. (2022)	Laboratory	Plunging jet	SSA number concentrations	Number Concentrations: Non-monotonic
10	Sellegri et al. (2023)	Laboratory	Plunging Jet	SSA number flux, Size resolved SSA number concentrations	Number Fluxes: Negative Number Concentrations: Non-monotonic
11	Hu et al. (2024)	Laboratory	Plunging Jet Plunging Waterfall	Size-resolved SSA number concentrations, surface bubble concentration	Jet Number Concentrations: Non-monotonic Waterfall Number Concentrations: Positive
12	Jaeglé et al. (2011)	Field	Global	Ship- & Station-based mass concentrations; MODIS & AERONET AOD; GEOS-Chem simulations	Mass Concentrations: Positive
13	Grythe et al. (2014)	Field	Global	Ship- & Station-based mass concentrations; FLEXPART simulations	Mass Concentrations: Positive
14	Lehahn et al. (2014)	Field	North Atlantic	Ship-based number concentrations	Number Concentrations: Negative
15	Ovadnevaite et al. (2014)	Field	North Atlantic	Ship-based number fluxes; station-based number	Number Fluxes: Positive

				concentrations; model-based wave parameters	
16	Saliba et al. (2019)	Field	North Atlantic	Ship-based number concentrations	Number Concentrations: Negative Mass Concentrations: Positive
17	Liu & Liu et al. (2021)	Field	Pacific & Atlantic	Airborne volume concentrations	Volume Concentrations: Positive
18	Markuszewski et al. (2024)	Field	North Atlantic, Baltic Sea	Ship-based number and volume fluxes	Number Fluxes: Negative (Baltic Sea all chlorophyll statistically significant) Volume Fluxes: Positive (Baltic Sea low chlorophyll statistically significant; Atlantic negative)
19	**This study**	**Laboratory**	**Wind-Wave Interactions (SOARS)**	**Number concentrations; number fluxes**	**Number concentrations: Negative (submicron), non-monotonic (supermicron)** **Number fluxes: Negative (submicron), non-monotonic (supermicron)** **Mass fluxes: Non-monotonic**

Table S1: Summary of previously documented SSA-SST relationships and method of investigation.

S2 Experimental Conditions

Experimental Summary		Channel Conditions		SSA Sample Conditions	
		SST Range	Salinity	RH	Flow Rate
Experiment	Dates	[°C]	[PSU]	[%]	[L min^{-1}]
Cooling	11 - 16 February 2024	2.2 - 20.0	36.4 ± 0.2	19 ± 4	6.2[a] 2.6[b]
Warming	17 February - 01 March 2024	2.5 - 23	36.2 ± 0.2	20 ± 3	6.2[a] 2.6[b]

Table S2: Summary of experimental conditions. Both experiments were conducted with filtered seawater filled to a channel depth of 1.2 m. Wind speed was 11 m s^{-1}. Wave stroke height was 0.42 m. [a] Sampling system consisting of 2x SMPS and 1x APS. [b] Sampling system consisting of SM, OPS, MAGIC CPC, NanoScan SMPS.

SSA particle number size distributions (PNSDs) are reported for equilibrium wind-wave conditions in SOARS. SOARS includes two makeup fans that maintain positive pressure within the channel and minimize room air contamination. To account for background aerosol concentrations and ensure minimal contamination, PNSDs were measured during each period shown in Fig. 1b in the main text. PNSDs of each period were measured across three days, each with an SST of 20 °C (Figure S1a-c). Multi-day mean PNSDs for each period are exhibited in Figure S1d and probability density functions (PDFs) of the multi-day mean PNSDs are shown in Figure S1e, demonstrating that Wind & Waves is distinct from the other events. The PNSDs observed during Wind & Waves have a similar bimodal shape as other laboratory measurements of SSA (Prather et al., 2013;

Stokes et al., 2013). The remaining events, Room Air, Aerosol Mode, and Wind Alone, show higher variability. This highlights two features: (1) SOARS' precision in generating SSA under wind-wave interactions (relative standard deviation of ~20% compared to ~50% for other conditions) and (2) that the SSA population produced by SOARS is minimally influenced by contamination. More information on the daily variability of PNSDs in SOARS across different wind speeds and wave fields is discussed in Leibensperger III et al. (2026). Further discussion of SSA measurement considerations is provided in Sect. S4.

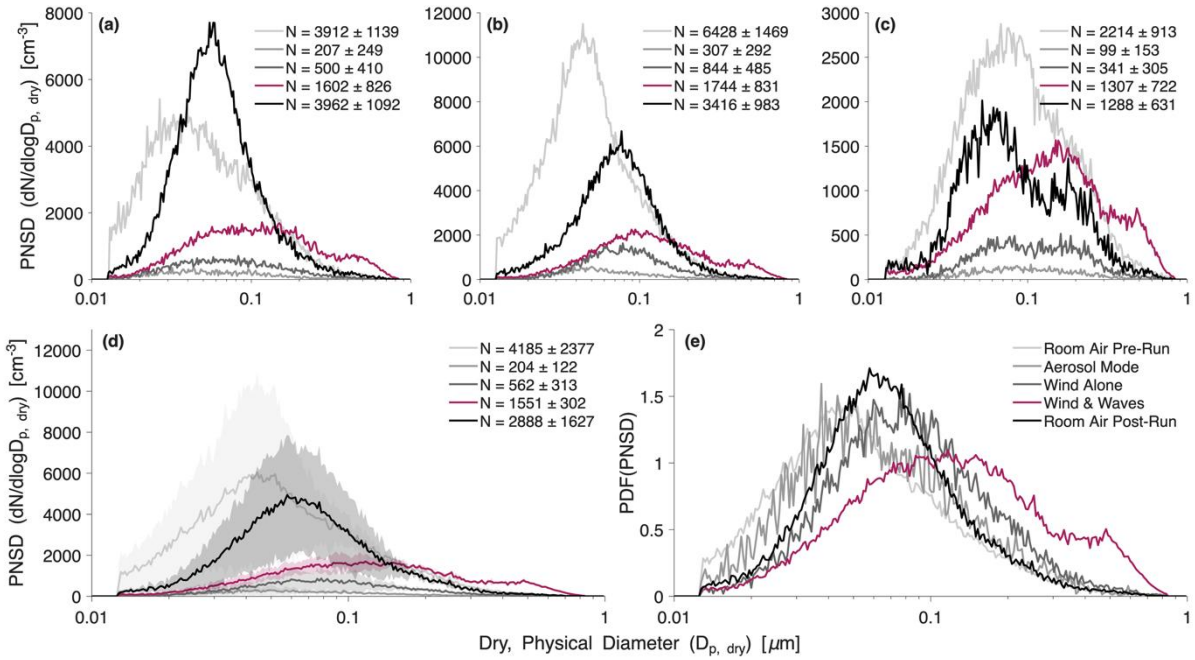

Figure S1: Assessment of daily variability of PNSDs across SOARS conditions. (a) Condition-averaged PNSDs for cooling experiment day 1, (b) cooling experiment day 2, and (c) warming experiment day 5. (d) 3-day average PNSDs across SOARS events. (e) Probability density function (PDF) of 3-day average PNSDs across SOARS events. Total number concentrations ± 1 standard deviation are shown in (a-d).

S3 Sea Spray Aerosol Sampling & Corrections

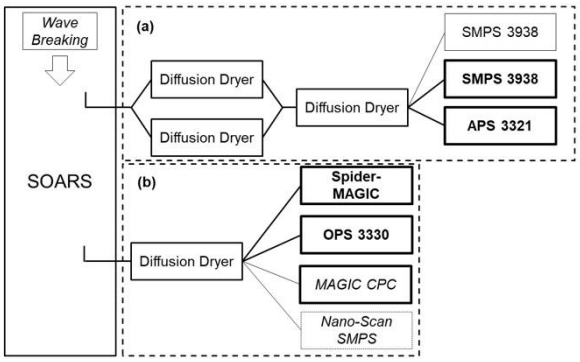

Figure S2: Sampling schematic. (a) Primary instruments and (b) secondary instruments. The sampling inlet of the secondary instruments (b) was positioned 2 m downstream of the primary instruments (a). Sampling lines were constructed of stainless steel and black conductive tubing. Sample inlets were positioned in the direction of wave breaking to achieve near-isoaxial sampling.

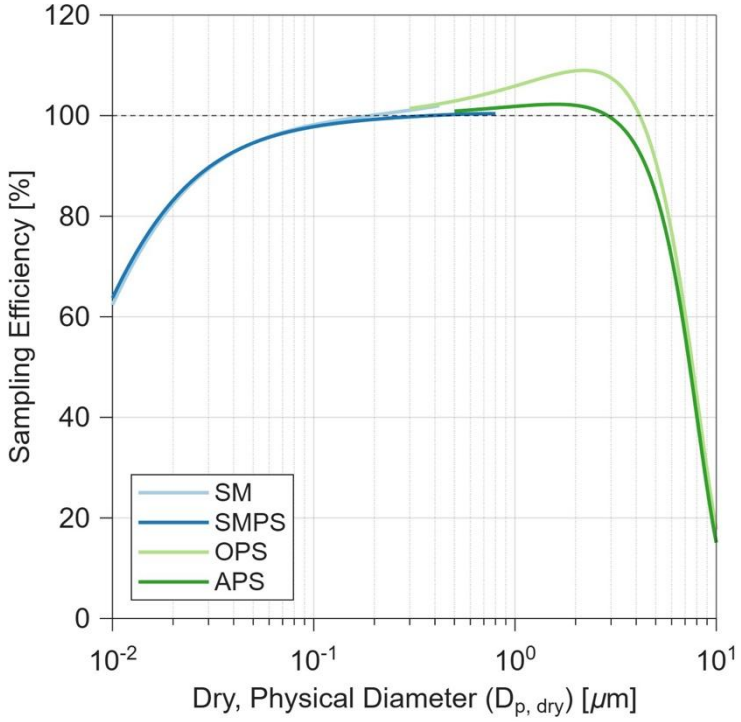

Figure S3: Assessment of particle losses within sampling lines. Sampling efficiency determined using the Particle Loss Calculator (PLC, Von Der Weiden et al., (2009)) for the aerosol sampling instruments used in this study.

S4 Measurement Considerations

SOARS allows for extensive controls of experimental variables; however, achieving SSTs near the upper and lower limits of its operational limit was time-intensive, reducing the number of data points achieved at the lowest and highest SSTs. Weighted least squares regressions were applied to reduce the influence of the number of runs within each SST bin. The weighting factor (w) is equal to the inverse of the measurement variance (σ^2):

$$\boldsymbol{w} = \frac{\mathbf{1}}{\boldsymbol{\sigma^2}}, \quad \text{(S1)}$$

The influence of weighted and unweighted least squares regressions is shown in Figure S4. Non-weighted regressions show high coefficients of determination ($R^2 \geq 0.92$, $p < 0.05$) for both linear and quadratic models, except for the supermicron linear model where only the quadratic model shows high coefficients of determination. Weighted least squares regression shows a slight improvement in performance ($R^2 \geq 0.97$, $p < 0.05$) due to the higher uncertainty associated with measurements at moderate SSTs (i.e., between 5 and 15 °C). The weighting process was applied to the analyses in the main text.

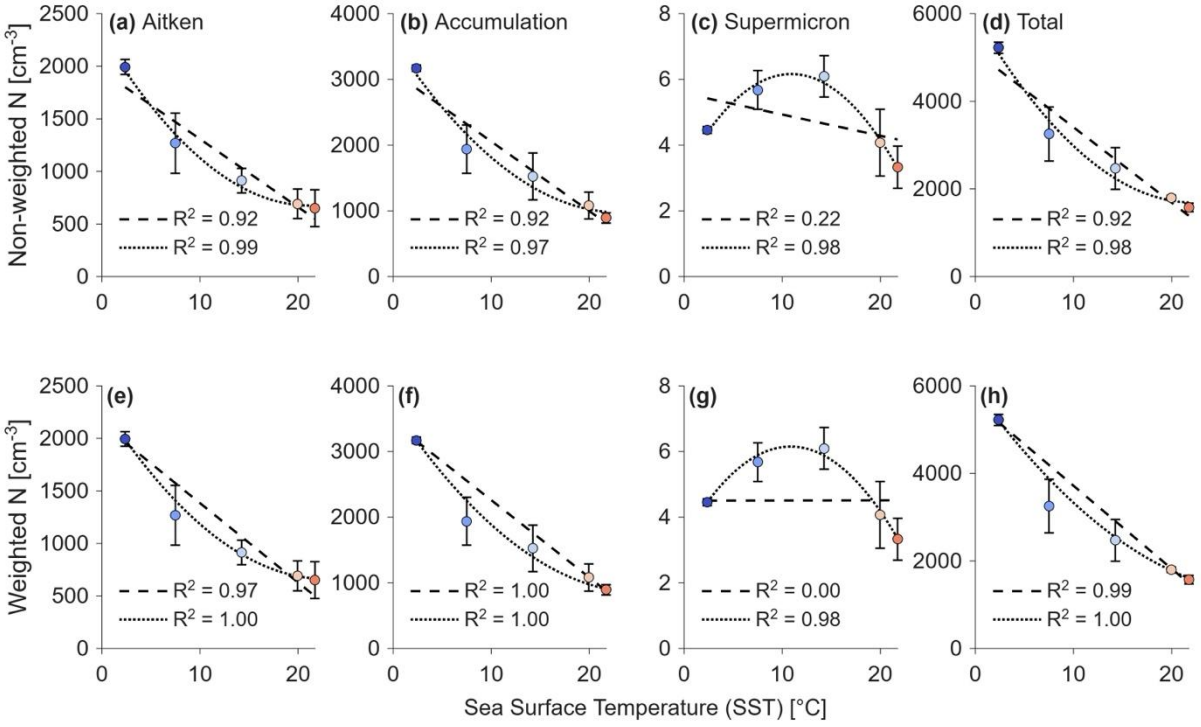

Figure S4: (top row) Non-weighted least squares regression based on Aitken, Accumulation, Supermicron and total number concentrations. (bottom row) Same as top row but weighted using Eq. S1. Linear models are shown by dashed lines, and quadratic models are shown by dotted lines.

The chosen methods for flux estimation in SOARS can introduce additional uncertainties. Figure S5 compares the submicron method (applying a linear regression to the initial rise of particle concentrations within the first five minutes) and the supermicron method (assuming production flux is equal to the product of steady-state concentrations and the loss rate measured

during the Decay period). The black lines indicate typical variability across three days from a separate SOARS experiment using the same wind speed, wave height, and filtering procedures as the current data. In panels (a, b), the solid lines indicate the chosen method, the dashed line indicates the non-chosen method, and the dotted lines indicate the chosen method corrected for by the typical ratio of the two methods. Data is shown for the coldest and warmest SSTs (2 and 23 °C) as bounds of the flux estimate variability. The solid lines are typically above the dotted lines, indicating that the chosen methods lead to a higher estimate of flux. These estimates (panel c) can be as high as a factor of about 20 (± 15) for typical SOARS conditions but remained within a factor of 6 for the SST-dependent results. While this uncertainty should not be overlooked, typical uncertainties in flux can be several orders of magnitude, indicating that our estimates are reasonable given the constraints and complexities of the system.

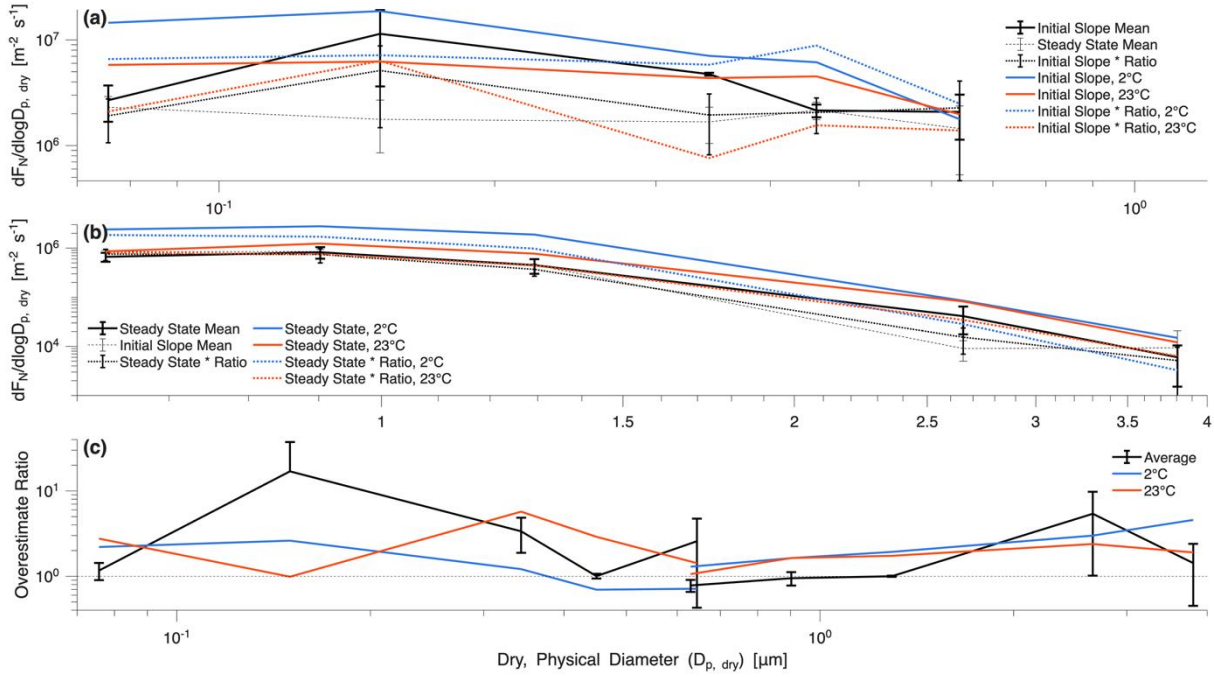

Figure S5. Comparison of flux estimation methods. (a) Comparison of methods in the submicron range for the coldest and warmest SSTs (blue and red) as well as a 3-day average from a separate SOARS campaign (black). Solid lines designate the chosen flux estimation method (initial rise for submicron), the dashed line is the other method (steady state for submicron), and dotted lines indicate the chosen method corrected based on the ratio between the two methods. (b) Same as (a), but for supermicron. Here the chosen method (solid lines) is steady state. (c) The overestimation ratio of the chosen method compared to the other method. The dashed line indicates a ratio of 1, or no overestimate.

S5 Theoretical Framework

The framework described in the main text relies on known quantities of subsurface bubbles (n) and surface bubbles (ñ) to estimate the net number of SSA of a given $D_{p,\,dry}$ that enters the atmosphere per square meter of ocean surface (N_0). Equation

8 summarizes the dependence of N on ñ, which is also time dependent. Equation S2 describes the change in concentration of ñ which is further dependent on the change in n (Eq. S3):

$$\frac{d\tilde{n}(r,t)}{dt} = Z * R(r) * n(r,t) - \big(B(r) + C(r) + D_2(r)\big) * \tilde{n}(r,t), \quad \text{(S2)}$$

$$\frac{dn(r,t)}{dt} = F(r) - \big(R(r) + D_3(r)\big) * n(r,t), \quad \text{(S3)}$$

Where Z is the depth of the subsurface bubble plume [m], R is the rate of breaching of subsurface bubbles on the surface [s^{-1}], C encompasses the rate of the net effects of surface bubble coalescence [s^{-1}], D_2 is the rate of dissolution of surface bubbles [s^{-1}], F is a function describing the formation of subsurface bubbles [$\#_{bubble}\ m^{-3}\ \mu m^{-1}\ s^{-1}$], and D_3 is the rate of subsurface bubbles lost to dissolution and removal [s^{-1}].

Equations S2 and S3 can be rearranged for ñ and n, respectively, which can then be substituted into Eq. 8 to solve for $\frac{dN_0}{dt}$. However, this method of solving the equations relies on knowledge of the concentration changes over time ($\frac{d\tilde{n}}{dt}$ & $\frac{dn}{dt}$), which can be determined experimentally in future studies.

Similar to Eqs. 9 and 10, here we document the dependencies of terms of Eqs. S2-S3 on SST. The rate at which subsurface bubbles breach the ocean surface (R) is known to be proportional to surface tension (γ) and inversely proportional to viscosity (ν) and solubility (κ) (Jaeglé et al., 2011; Nielsen and Bilde, 2020; Ovadnevaite et al., 2014; Sellegri et al., 2023; Song et al., 2023; Zábori et al., 2012):

$$R(r) \propto \frac{\gamma}{\nu\kappa}, \quad \text{(S4)}$$

Surface bubble coalescence (C) could be positive or negative, depending on the net effects of combining bubbles and shifting the bubble size distribution. C is expected to be primarily related to the size and number of surface bubbles, the area over which they extend, and γ holding bubbles together:

$$C(r) \propto \gamma^{-1}, \quad \text{(S5)}$$

The rate of subsurface bubbles lost to dissolution and removal (D_3) and the rate of dissolution of surface bubbles (D_2) are expected to be proportional to solubility (κ) and viscosity (ν), but inversely proportional to surface tension (γ) (Song et al., 2023; Zábori et al., 2012). Additionally, surface bubble dissolution is likely to be small, instead favouring bubble coalescence or bursting.

$$D_2(r) \propto \frac{\kappa\nu}{\gamma} \ll 1, \quad \text{(S6)}$$

$$D_3(r) \propto \frac{\kappa\nu}{\gamma}, \quad \text{(S7)}$$

The subsurface bubble formation rate is proportional to air entrainment (ε) (Callaghan et al., 2014):

$$F(r) \propto \varepsilon, \quad \text{(S8)}$$

S6 Particle Number Size Distributions

To ensure the conclusions of this study do not include artifacts caused by choice of instrument, we briefly compare the PNSDs across SSTs between the two setups of instruments (Figure S6). The SMPS-APS (top row) are the measurements used in the rest of the paper. The SM-OPS (bottom row) have a different overlap region and size bin resolution. While this leads to slight changes in the PNSD shape, the general suppression of SSA concentrations with increasing SST remains consistent. Additionally, the PNSD properties (D_g, σ_g, D_{mode}, and N) show consistent trends between all four instruments (Table S3).

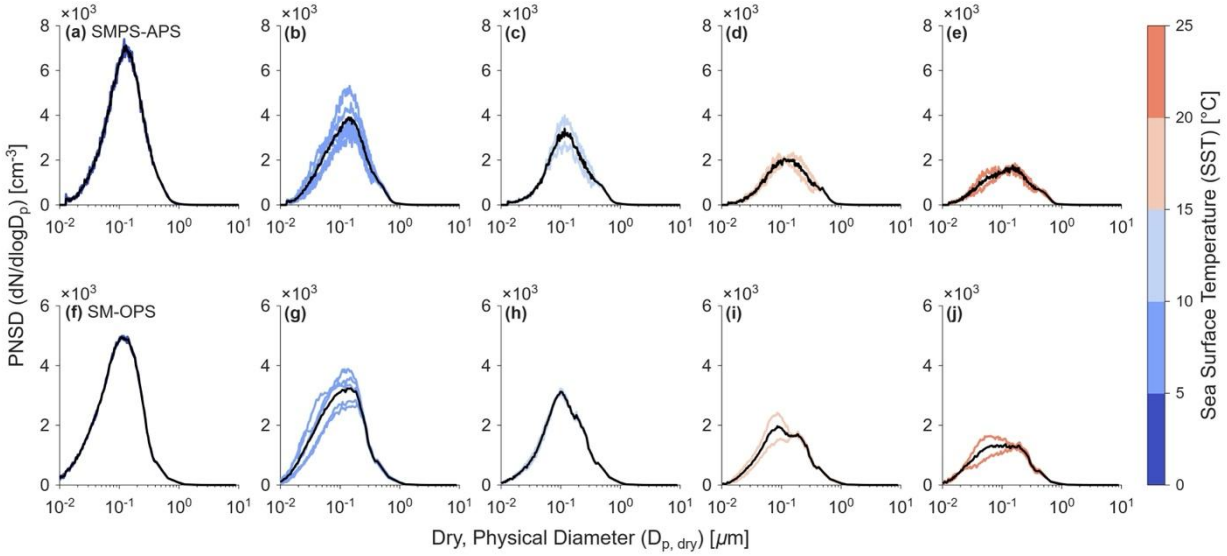

Figure S6: Individual run PNSDs separated by instrument (rows) and SST bin (columns). Steady-state PNSDs for each SST experimental run across five ranges:(right to left) 0-5 °C, 5-10 °C, 10-15 °C, 15-20 °C, 20-25 °C. (top row) SMPS-APS measurements and (bottom row) SM-OPS measurements. Mean PNSDs for each SST range are shown by a black line.

SST [°C]	D_g [µm]		σ_g		D_{mode} [µm]		N [cm^{-3}]	
-	SMPS-APS	SM-OPS	SMPS-APS	SM-OPS	SMPS-APS	SM-OPS	SMPS-APS	SM-OPS
2.4 ± 0.2	0.1119 ± 0.0011	0.0938 ± 0.0003	1.97 ± 0.02	2.216 ± 0.001	0.1343 ± 0.0011	0.116 ± 0.004	5222 ± 127	4289.1 ± 0.4
8 ± 2	0.110 ± 0.008	0.096 ± 0.009	2.06 ± 0.04	2.28 ± 0.04	0.142 ± 0.008	0.129 ± 0.014	3254 ± 613	3212 ± 527
14.25 ± 0.07	0.114 ± 0.005	0.104 ± 0.003	1.98 ± 0.04	2.168 ± 0.019	0.1185 ± 0.0011	0.103 ± 0.004	2471 ± 476	2534 ± 85
19.95 ± 0.07	0.112 ± 0.017	0.104 ± 0.015	2.04 ± 0.02	2.202 ± 0.003	0.136 ± 0.042	0.13 ± 0.05	1798 ± 61	1828 ± 309
22 ± 2	0.104 ± 0.014	0.091 ± 0.003	2.162 ± 0.005	2.40 ± 0.11	0.134 ± 0.044	0.11 ± 0.05	1576 ± 96	1514 ± 332

Table S3: Summary of binned results. An additional significant digit is retained when the last significant digit is 1.

S7 Parameters of the Particle Number Size Distribution

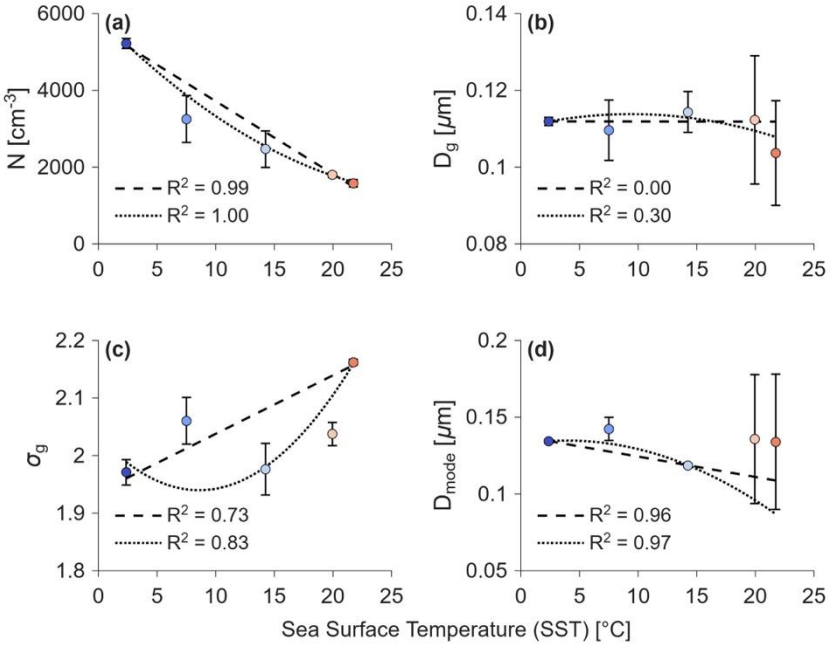

Figure S7: Key parameters of the SST-binned, uncertainty-weighted PNSDs. Parameters of the particle number size distribution include: (a) total number concentration, N, (b) geometric mean diameter, D_g, (c) geometric standard deviation, σ_g, and (d) mode diameter, D_{mode}. Linear (dashed) and quadratic (dotted) best-fit lines are shown in each panel. Error bars represent 1 standard deviation.

S8 Sea Spray Aerosol Mode Fitting

Aerosol size distributions have been previously described by a tri-modal scheme (Dedrick et al., 2024; Modini et al., 2015; Williams et al., 2024). Here, we separate the PNSDs, PNFDs, and PMFDs at the extreme temperatures in a tri-modal scheme comprised of the Aitken (≤ 0.1 μm), accumulation (0.1-1 μm), and supermicron (≥ 1 μm) modes as described in the main text. Table S4 describes the results of tri-modal fitting on the lowest (0-5 °C) and highest (20-25 °C) SST bins as well as the difference between them.

SST [°C]	Aitken			Accumulation			Supermicron		
PNSD	**N [cm^{-3}]**	**D_g [μm]**	**σ_g**	**N [cm^{-3}]**	**D_g [μm]**	**σ_g**	**N [cm^{-3}]**	**D_g [μm]**	**σ_g**
0-5	500	0.038	1.65	4468	0.130	1.82	142	0.416	1.61
20-25	325	0.046	1.71	1132	0.154	1.83	91	0.423	1.68
Difference	-175	0.008	0.06	-3336	0.024	0.02	-51	0.007	0.07

PNFD	F_N ($\times 10^6$) [m^{-2} s^{-1}]	D_g [µm]	σ_g	F_N ($\times 10^6$) [m^{-2} s^{-1}]	D_g [µm]	σ_g	F_N ($\times 10^6$) [m^{-2} s^{-1}]	D_g [µm]	σ_g
0-5	5.613	0.055	1.80	5.009	0.171	1.80	0.3995	0.800	1.55
20-25	1.010	0.043	1.40	2.090	0.151	1.83	1.772	0.800	1.54
Difference	-4.603	-0.012	-0.40	-2.919	-0.021	0.03	1.373	0	-0.02
PMFD	**F_M ($\times 10^{-12}$) [kg m^{-2} s^{-1}]**	**D_g [µm]**	**σ_g**	**F_M ($\times 10^{-10}$) [kg m^{-2} s^{-1}]**	**D_g [µm]**	**σ_g**	**F_M ($\times 10^{-8}$) [kg m^{-2} s^{-1}]**	**D_g [µm]**	**σ_g**
0-5	3.094	0.068	1.80	8.175	0.360	1.80	0.579	1.073	1.66
20-25	0.1639	0.035	1.32	0.6028	0.199	1.60	1.570	1.542	1.76
Difference	-2.930	-0.033	-0.48	-7.572	-0.161	-0.20	0.990	0.471	0.10

Table S4: Magnitude, geometric mean diameter, and geometric standard deviation information for tri-modal fitting to temperature extremes PNSDs, PNFDs, and PMFDs. The difference is computed as the warmer SST (20-25 °C) minus the cooler SST (0-5 °C).

S9 Higher-Order Size Distributions

Laboratory measurements of SSA are influenced by the breaking wave proxy. In this study, SOARS was operated with continuously recirculating winds, unlike previous studies, which employed flow-through systems (Christiansen et al., 2019; Hu et al., 2024; Sauer et al., 2022). A thorough analysis comparing flow-through and well-mixed SSA generators is beyond the scope of this work, so we provide probability density functions (PDF) of measured size distributions (Figure S8) to aid in comparisons to other breaking wave proxies. Particle number, surface area, and volume size distributions can be reconstructed by the interested reader using the total number, surface area, and volume estimates included in the legends. The prevalence of the secondary mode at the warmest SSTs accounts for the differences in PDF shapes.

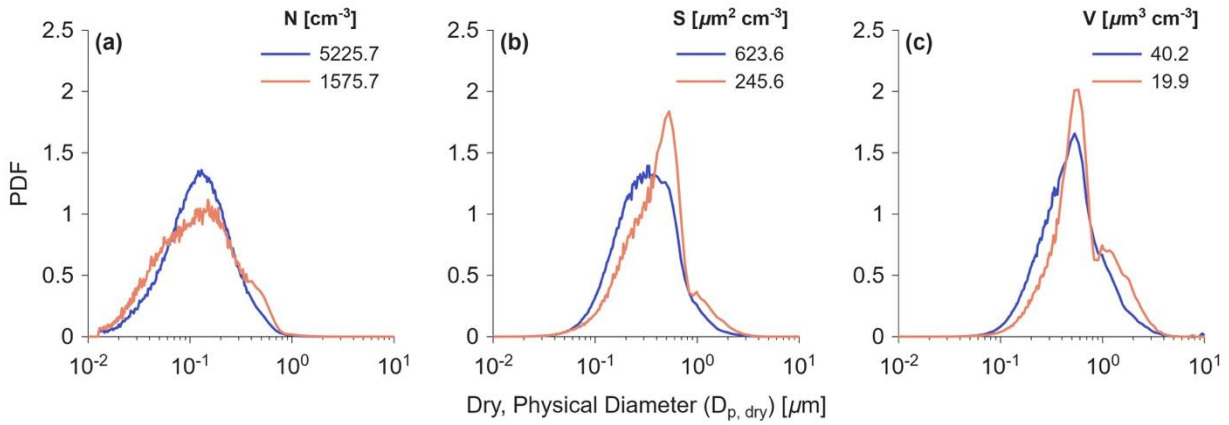

Figure S8: Probability density functions of extreme SST higher order size distributions. PDF of (a) number, (b) surface area, and (c) volume size distributions at the lowest and highest SST. PDFs are normalized by the total concentrations indicated in each respective legend.

Sea spray aerosols are the largest natural source of aerosol mass, and changing sea surface temperature, as shown here, will have profound effects on Earth's climate (Grythe et al., 2014; de Leeuw et al., 2011; Lewis and Schwartz, 2004). Figure S9 demonstrates that shifts in SST will have size-dependent effects on the mass of SSA produced.

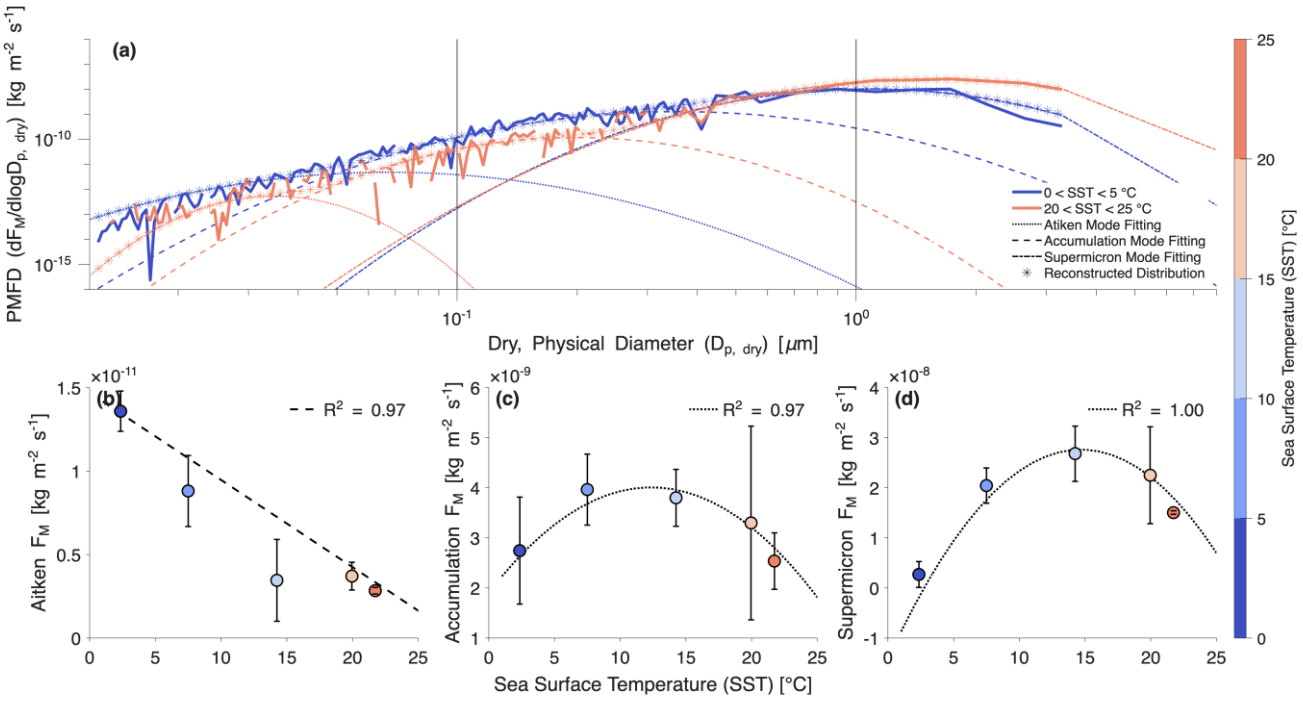

Figure S9: Evaluation of particle mass flux trends. Particle mass flux distributions (a) for the warmest and coldest SST bins. Accompanying mode fitting included. Total mass flux as a function of SST for Aitken mode (b), accumulation mode (c), and supermicron (d) SSA.

S10 Experiment Comparisons

The analysis and figures of the main text condense measurements across the two experiments for simplicity and to account for the daily variability of the system. The experimental differences for modal number concentrations (N, Figure S10), total number, surface area, and volume (Figure S11), loss rates (Figure S12), modal number flux (F_N, Figure S13), modal mass flux (F_M, Figure S14) and correction factors (CFs, Figure S15) are included here.

Combining cooling and warming total number concentrations improves the linear regression R^2 for the Aitken mode, accumulation mode, and total number and improves the quadratic regression R^2 for the supermicron mode. The SST-binned data reported in the main text is shown in the right column of Figure S10, along with data used for each bin. Similarly, Figure S11 shows total number, surface area, and volume concentrations for cooling, warming, and combined experiments. All

regressions produce high R^2 values ($R^2 > 0.85$) and binning data does not influence the overall trend as SST increases. Furthermore, all regression R^2 values are statistically significant above the 95 % confidence level

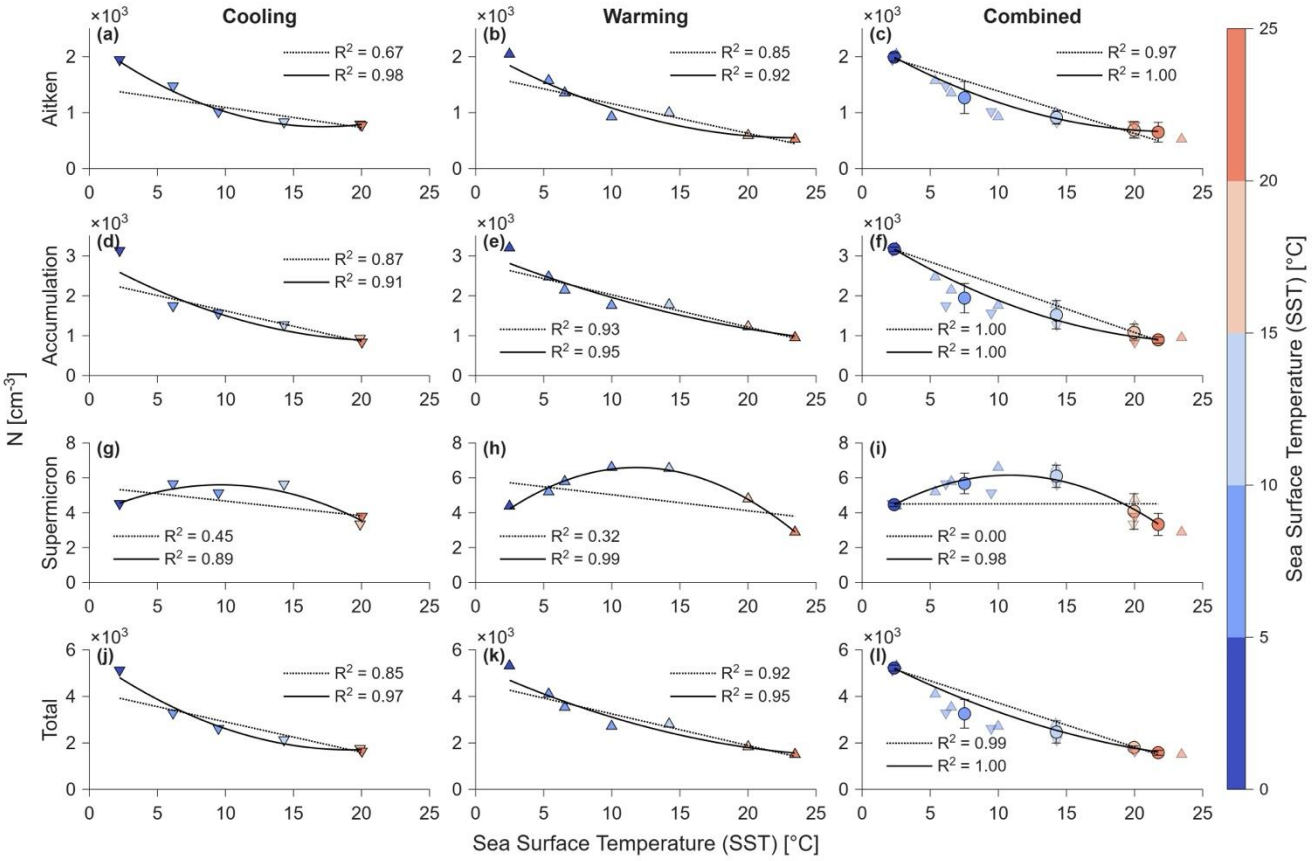

Figure S10: Total number concentration by experiment (columns) and size range (rows). SSA Number Concentrations by Mode. SSA concentrations for the Aitken, Accumulation, Supermicron modes, and total number concentration for the (a, d, g, j) Cooling experiment, (b, e, h, k) Warming experiment, and (c, f, i, l) Combined experiments. Binned averages are shown by circular markers with error bars representing one standard deviation.

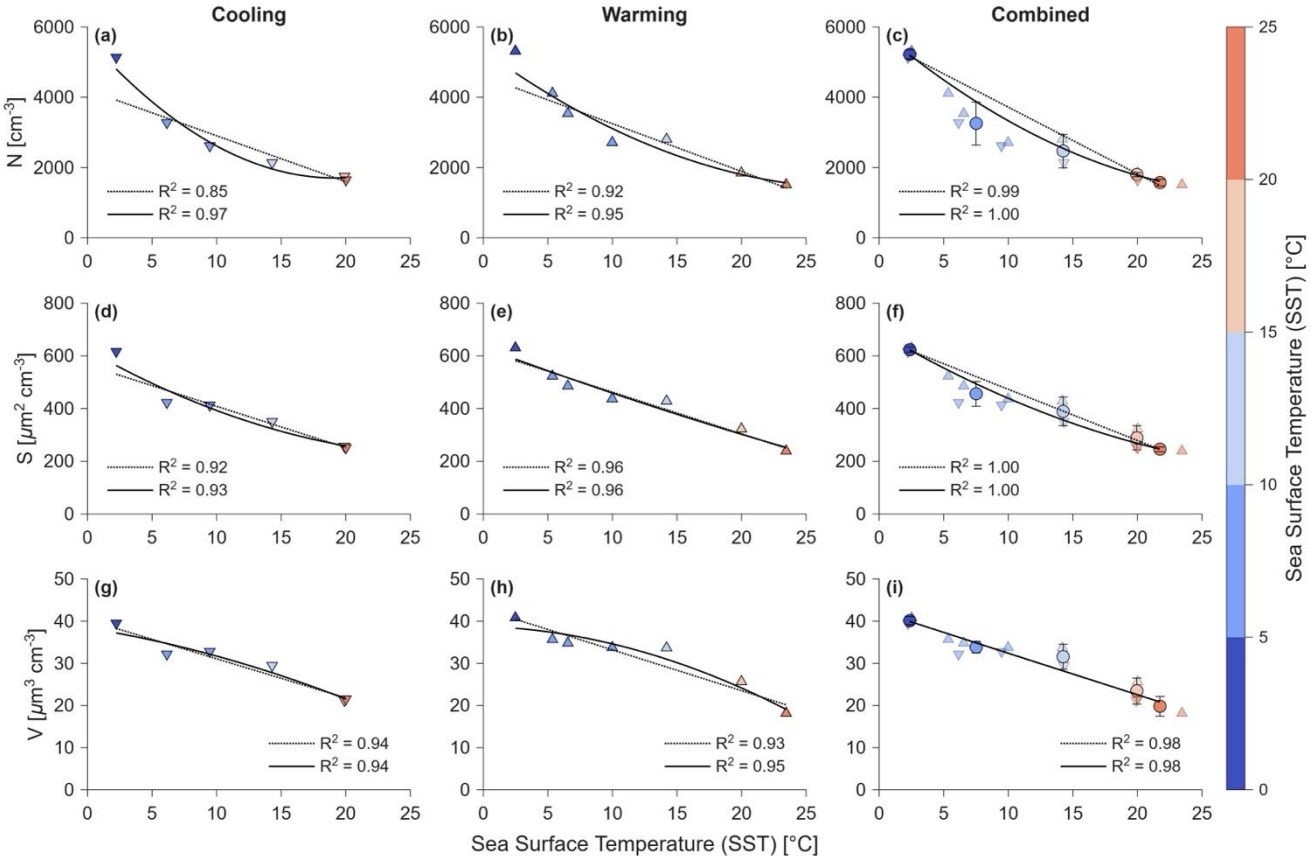

Figure S11: Total number concentration, surface area, and volume (rows) by experiment (columns). SSA Number, Surface Area, and Volume for the (a, d, g, j) Cooling experiment, (b, e, h, k) Warming experiment, and (c, f, i l) Combined experiments. Binned averages are shown by circular markers with error bars representing one standard deviation.

235 The loss rates do not appear to be different between the cooling and warming experiments (Figure S12). However, during both experiments the aerosol loss rates measured during the coldest SSTs (SST < 5 °C) are consistently and dramatically less than for the other SSTs across all sizes. This indicates that the loss rates measured here are likely sensitive to subtle, hard-to-detect modifications in the SOARS system that affect turbulence. Future SOARS aerosol studies would benefit from additional loss rate characterization.

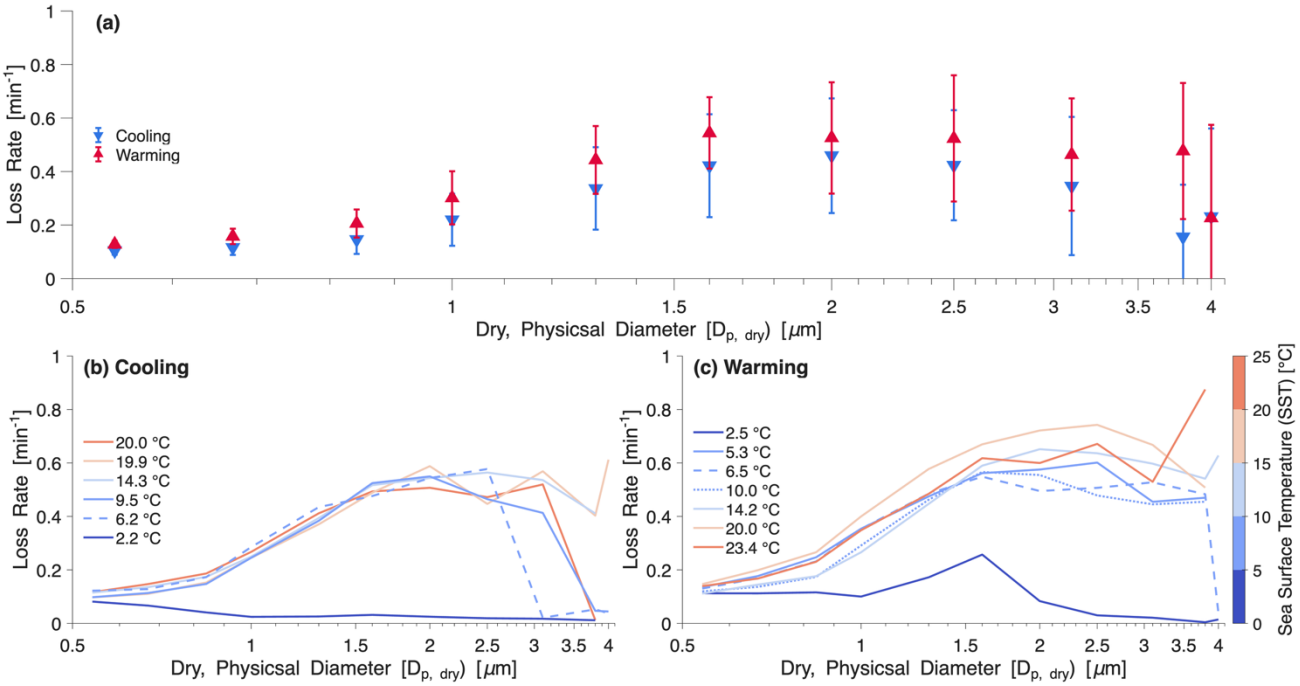

Figure S12: Size-resolved and SST-dependent loss rates. (a) Experimental average ± standard deviation loss rate estimates as functions of SSA diameter. (b) Size distributions of loss rates for each SST during the cooling experiment. (c) same as (b) for the warming experiment.

The F_N and F_M analyses were separated by experiment and into the Aitken, accumulation, and supermicron modes, along with total flux. Figure S13 showcases the separation of number flux and Figure S14 showcases the separation of mass flux where the SST-binned best-fit line from the main text figures is included as a bolded line in the combined column (panels c, f, i, and l) of each figure, coplotted with the combined, non-SST-binned measurements and their corresponding linear (dashed lines) and quadratic (dotted lines) regressions. It is important to note that the R^2 value for the temperature-binned data is close to 1 due to the limited number of input data points (n = 5), however, the regression of the temperature-binned data closely aligns with the regression of the combined data points from both experiments (n = 13). While the regressions and figures in the main text are simplified versions to aid in clarity, they represent the trends well despite the low number of input data points.

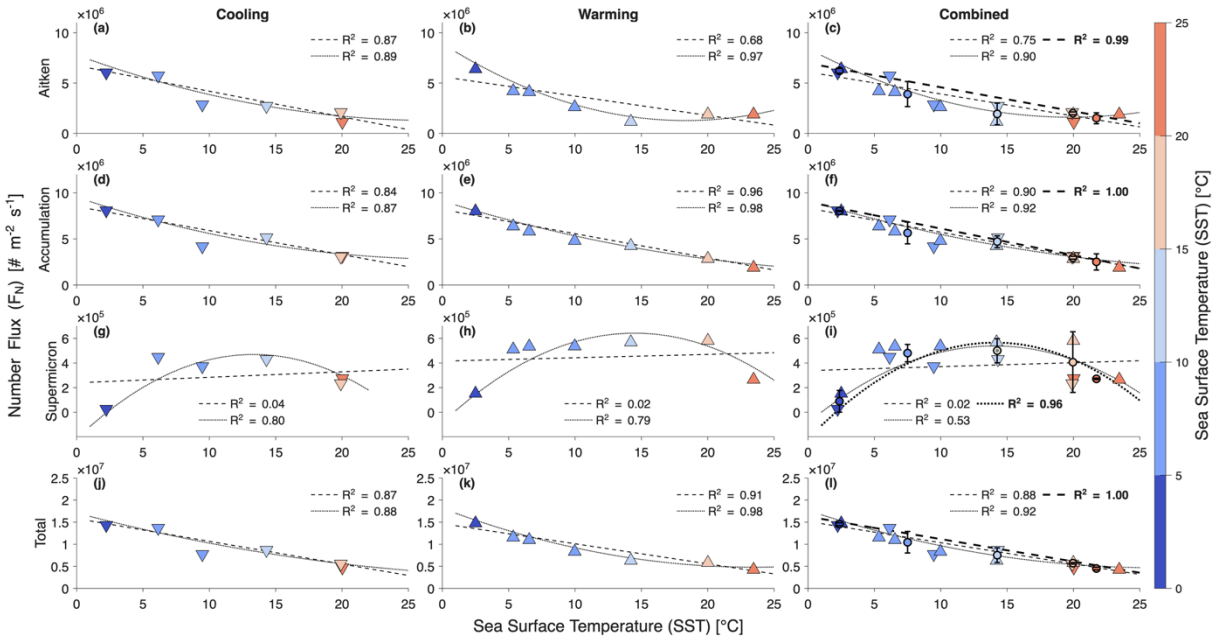

Figure S13: Total number flux (F_N) by experiment (columns) and size range (rows). Dashed lines indicate linear regressions, and dotted lines indicate quadratic regressions. The recommended regression based on temperature-binned data is included in panels c, f, i, and l as bolded lines.

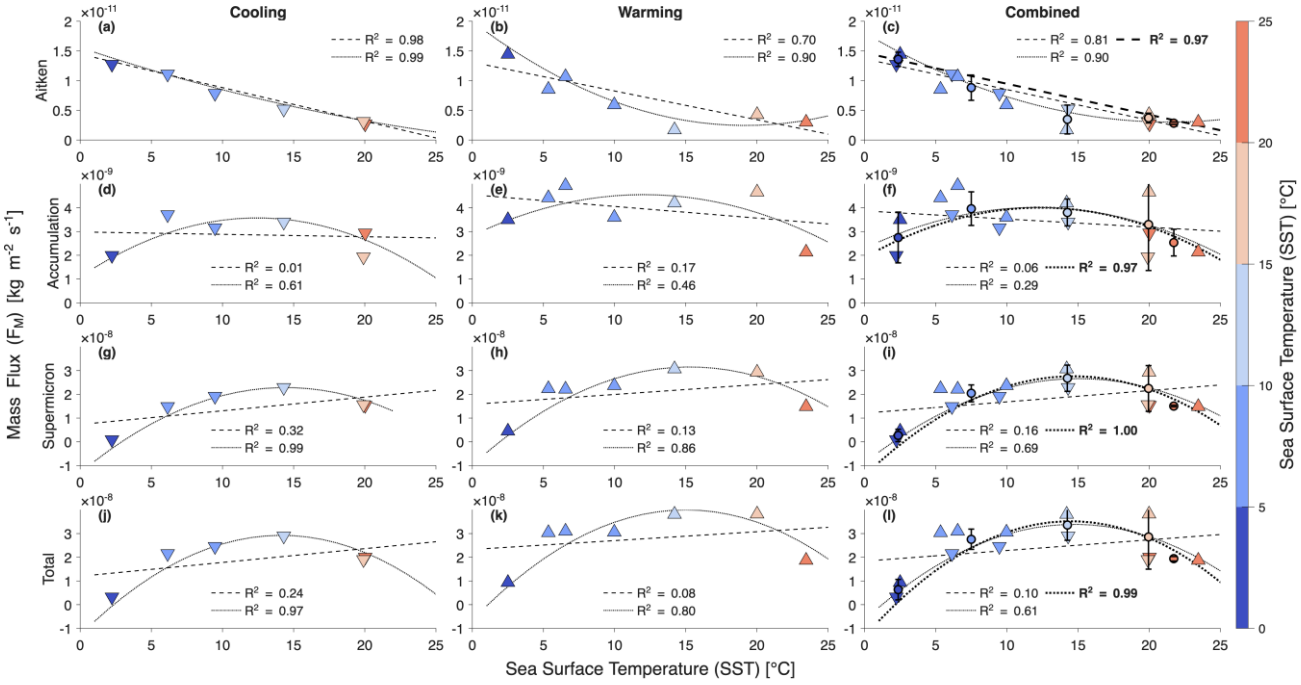

Figure S14: Total mass flux (F_M) by experiment (columns) and size range (rows). Dashed lines indicate linear regressions, and dotted lines indicate quadratic regressions. The recommended regression based on temperature-binned data is included in panels c, f, i, and l as bolded lines.

Finally, the CF analysis from the main text (Sect. 3.6) was repeated for the cooling and warming experiments individually to identify how SST hysteresis influenced the CFs. Importantly, the cooling and warming linear CF_N regressions capture the overall trends well ($R^2 = 0.87$, $p < 0.05$ for the cooling CF_N and $R^2 = 0.91$, $p << 0.01$ for the warming CF_N). Similarly, the quadratic CF_M regressions capture the overall trends well for each experiment ($R^2 = 0.97$, $p < 0.01$ for the cooling CF_M, $R^2 = 0.80$, $p < 0.05$ for the warming CF_M). Additionally, if future studies are interested, size-resolved SST-dependent CFs could be calculated from the size-resolved PNFDs and PMFDs.

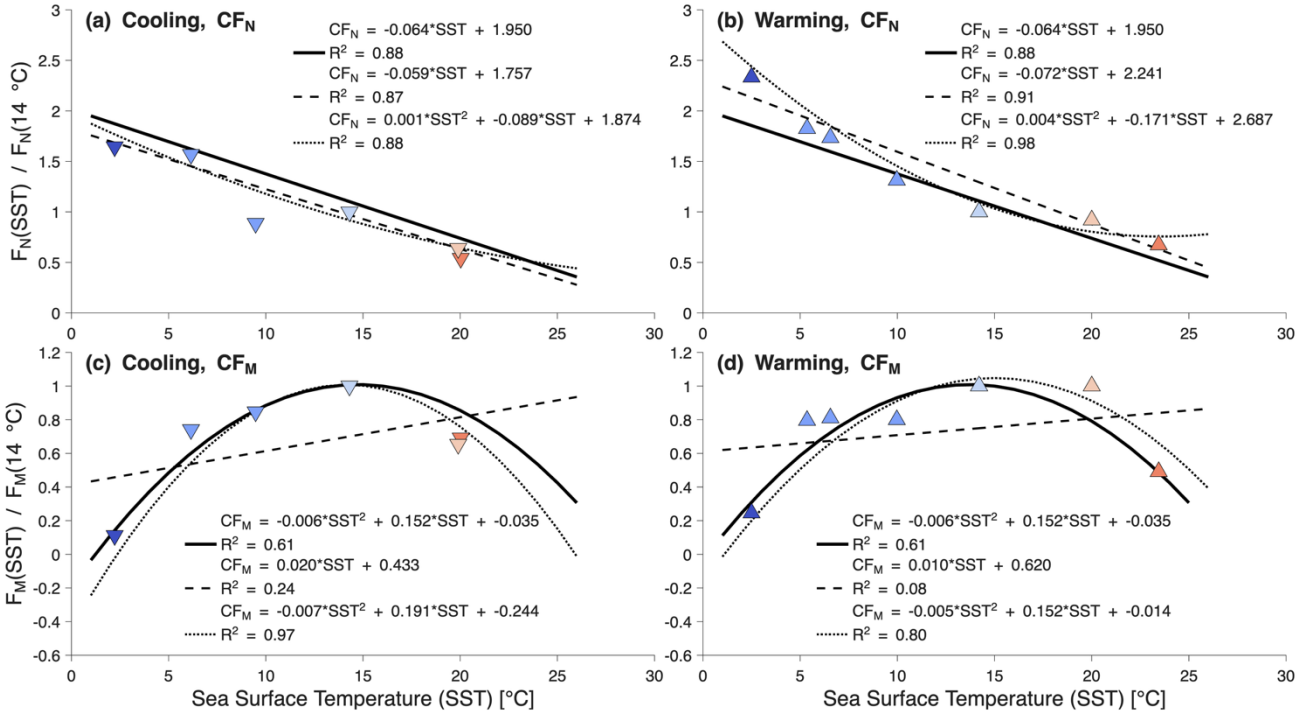

Figure S15: Correction factors by experiment. Number flux correction factors for the cooling (a) and warming (b) experiments. Mass flux correction factors for the cooling (c) and warming (d) experiments. The suggested CFs from Figure 8 in the main text are included as solid lines and the top equation in each panel.

References

Callaghan, A. H., Stokes, M. D., and Deane, G. B.: The effect of water temperature on air entrainment, bubble plumes, and surface foam in a laboratory breaking-wave analog, Journal of Geophysical Research: Oceans, 119, 7463–7482, https://doi.org/10.1002/2014JC010351, 2014.

Christiansen, S., Salter, M. E., Gorokhova, E., Nguyen, Q. T., and Bilde, M.: Sea Spray Aerosol Formation: Laboratory Results on the Role of Air Entrainment, Water Temperature, and Phytoplankton Biomass, Environ. Sci. Technol., 53, 13107–13116, https://doi.org/10.1021/acs.est.9b04078, 2019.

Dedrick, J. L., Russell, L. M., Sedlacek III, A. J., Kuang, C., Zawadowicz, M. A., and Lubin, D.: Aerosol-Correlated Cloud Activation for Clean Conditions in the Tropical Atlantic Boundary Layer During LASIC, Geophysical Research Letters, 51, e2023GL105798, https://doi.org/10.1029/2023GL105798, 2024.

Forestieri, S. D., Moore, K. A., Martinez Borrero, R., Wang, A., Stokes, M. D., and Cappa, C. D.: Temperature and Composition Dependence of Sea Spray Aerosol Production, Geophysical Research Letters, 45, 7218–7225, https://doi.org/10.1029/2018GL078193, 2018.

Grythe, H., Ström, J., Krejci, R., Quinn, P., and Stohl, A.: A review of sea-spray aerosol source functions using a large global set of sea salt aerosol concentration measurements, Atmospheric Chemistry and Physics, 14, 1277–1297, https://doi.org/10.5194/acp-14-1277-2014, 2014.

Hu, J., Li, J., Tsona Tchinda, N., Song, Y., Xu, M., Li, K., and Du, L.: Underestimated role of sea surface temperature in sea spray aerosol formation and climate effects, npj Clim Atmos Sci, 7, 1–12, https://doi.org/10.1038/s41612-024-00823-x, 2024.

Jaeglé, L., Quinn, P. K., Bates, T. S., Alexander, B., and Lin, J.-T.: Global distribution of sea salt aerosols: new constraints from in situ and remote sensing observations, Atmospheric Chemistry and Physics, 11, 3137–3157, https://doi.org/10.5194/acp-11-3137-2011, 2011.

de Leeuw, G., Andreas, E. L., Anguelova, M. D., Fairall, C. W., Lewis, E. R., O'Dowd, C., Schulz, M., and Schwartz, S. E.: Production flux of sea spray aerosol, Reviews of Geophysics, 49, https://doi.org/10.1029/2010RG000349, 2011.

Lehahn, Y., Koren, I., Rudich, Y., Bidle, K. D., Trainic, M., Flores, J. M., Sharoni, S., and Vardi, A.: Decoupling atmospheric and oceanic factors affecting aerosol loading over a cluster of mesoscale North Atlantic eddies, Geophysical Research Letters, 41, 4075–4081, https://doi.org/10.1002/2014GL059738, 2014.

Leibensperger III, R. J., Deane, G. B., Lee, C., Harb, C., Stokes, M. D., Kimble, K. A., Andreae, M. O., Herbst, J. K., Pham, E., Hamlin, J. D., Sandstrom, G., Pogue, E. A., and Prather, K. A.: Novel Sea Spray Aerosol Measurements Using the Scripps Ocean-Atmosphere Research Simulator (SOARS), Journal of Geophysical Research: Atmospheres, 131, e2025JD044254, https://doi.org/10.1029/2025JD044254, 2026.

Lewis, E. R. and Schwartz, S. E.: Sea Salt Aerosol Production Mechanisms, Methods, Measurements and Models, Washington DC, 2004.

Liu, S., Liu, C. C., Froyd, K. D., Schill, G. P., Murphy, D. M., Bui, T. P., Dean-Day, J. M., Weinzierl, B., Dollner, M., Diskin, G. S., Chen, G., and Gao, R. S.: Sea spray aerosol concentration modulated by sea surface temperature, Proceedings of the National Academy of Sciences of the United States of America, 118, 3–8, https://doi.org/10.1073/pnas.2020583118, 2021.

Markuszewski, P., Nilsson, E. D., Zinke, J., Mårtensson, E. M., Salter, M., Makuch, P., Kitowska, M., Niedźwiecka-Wróbel, I., Drozdowska, V., Lis, D., Petelski, T., Ferrero, L., and Piskozub, J.: Multi-year gradient measurements of sea spray fluxes

over the Baltic Sea and the North Atlantic Ocean, Atmospheric Chemistry and Physics, 24, 11227–11253, https://doi.org/10.5194/acp-24-11227-2024, 2024.

Mårtensson, E. M., Nilsson, E. D., de Leeuw, G., Cohen, L. H., and Hansson, H.-C.: Laboratory simulations and parameterization of the primary marine aerosol production, Journal of Geophysical Research: Atmospheres, 108, https://doi.org/10.1029/2002JD002263, 2003.

Modini, R. L., Frossard, A. A., Ahlm, L., Russell, L. M., Corrigan, C. E., Roberts, G. C., Hawkins, L. N., Schroder, J. C., Bertram, A. K., Zhao, R., Lee, A. K. Y., Abbatt, J. P. D., Lin, J., Nenes, A., Wang, Z., Wonaschütz, A., Sorooshian, A., Noone, K. J., Jonsson, H., Seinfeld, J. H., Toom-Sauntry, D., Macdonald, A. M., and Leaitch, W. R.: Primary marine aerosol-cloud interactions off the coast of California, Journal of Geophysical Research: Atmospheres, 120, 4282–4303, https://doi.org/10.1002/2014JD022963, 2015.

Nielsen, L. S. and Bilde, M.: Exploring controlling factors for sea spray aerosol production: temperature, inorganic ions and organic surfactants, Tellus B: Chemical and Physical Meteorology, 72, 1–10, https://doi.org/10.1080/16000889.2020.1801305, 2020.

Ovadnevaite, J., Manders, A., de Leeuw, G., Ceburnis, D., Monahan, C., Partanen, A.-I., Korhonen, H., and O'Dowd, C. D.: A sea spray aerosol flux parameterization encapsulating wave state, Atmos. Chem. Phys., 14, 1837–1852, https://doi.org/10.5194/acp-14-1837-2014, 2014.

Prather, K. A., Bertram, T. H., Grassian, V. H., Deane, G. B., Stokes, M. D., DeMott, P. J., Aluwihare, L. I., Palenik, B. P., Azam, F., Seinfeld, J. H., Moffet, R. C., Molina, M. J., Cappa, C. D., Geiger, F. M., Roberts, G. C., Russell, L. M., Ault, A. P., Baltrusaitis, J., Collins, D. B., Corrigan, C. E., Cuadra-Rodriguez, L. A., Ebben, C. J., Forestieri, S. D., Guasco, T. L., Hersey, S. P., Kim, M. J., Lambert, W. F., Modini, R. L., Mui, W., Pedler, B. E., Ruppel, M. J., Ryder, O. S., Schoepp, N. G., Sullivan, R. C., and Zhao, D.: Bringing the ocean into the laboratory to probe the chemical complexity of sea spray aerosol, Proceedings of the National Academy of Sciences of the United States of America, 110, 7550–7555, https://doi.org/10.1073/pnas.1300262110, 2013.

Saliba, G., Chen, C.-L., Lewis, S., Russell, L. M., Rivellini, L.-H., Lee, A. K. Y., Quinn, P. K., Bates, T. S., Haëntjens, N., Boss, E. S., Karp-Boss, L., Baetge, N., Carlson, C. A., and Behrenfeld, M. J.: Factors driving the seasonal and hourly variability of sea-spray aerosol number in the North Atlantic, Proceedings of the National Academy of Sciences, 116, 20309–20314, https://doi.org/10.1073/pnas.1907574116, 2019.

Salter, M. E., Nilsson, E. D., Butcher, A., and Bilde, M.: On the seawater temperature dependence of the sea spray aerosol generated by a continuous plunging jet, Journal of Geophysical Research: Atmospheres, 119, 9052–9072, https://doi.org/10.1002/2013JD021376, 2014.

Salter, M. E., Zieger, P., Acosta Navarro, J. C., Grythe, H., Kirkevåg, A., Rosati, B., Riipinen, I., and Nilsson, E. D.: An empirically derived inorganic sea spray source function incorporating sea surface temperature, Atmospheric Chemistry and Physics, 15, 11047–11066, https://doi.org/10.5194/acp-15-11047-2015, 2015.

Sauer, J. S., Mayer, K. J., Lee, C., Alves, M. R., Amiri, S., Bahaveolos, C. J., Franklin, E. B., Crocker, D. R., Dang, D., Dinasquet, J., Garofalo, L. A., Kaluarachchi, C. P., Kilgour, D. B., Mael, L. E., Mitts, B. A., Moon, D. R., Moore, A. N., Morris, C. K., Mullenmeister, C. A., Ni, C.-M., Pendergraft, M. A., Petras, D., Simpson, R. M. C., Smith, S., Tumminello, P. R., Walker, J. L., DeMott, P. J., Farmer, D. K., Goldstein, A. H., Grassian, V. H., Jaffe, J. S., Malfatti, F., Martz, T. R., Slade, J. H., Tivanski, A. V., Bertram, T. H., Cappa, C. D., and Prather, K. A.: The Sea Spray Chemistry and Particle Evolution study (SeaSCAPE): overview and experimental methods, Environ. Sci.: Processes Impacts, 24, 290–315, https://doi.org/10.1039/D1EM00260K, 2022.

Sellegri, K., Barthelmeß, T., Trueblood, J., Cristi, A., Freney, E., Rose, C., Barr, N., Harvey, M., Safi, K., Deppeler, S., Thompson, K., Dillon, W., Engel, A., and Law, C.: Quantified effect of seawater biogeochemistry on the temperature dependence of sea spray aerosol fluxes, Atmospheric Chemistry and Physics, 23, 12949–12964, https://doi.org/10.5194/acp-23-12949-2023, 2023.

Sofieva, S., Asmi, E., Atanasova, N. S., Heikkinen, A. E., Vidal, E., Duplissy, J., Romantschuk, M., Kouznetsov, R., Kukkonen, J., Bamford, D. H., Hyvärinen, A.-P., and Sofiev, M.: Effects of temperature and salinity on bubble-bursting aerosol formation simulated with a bubble-generating chamber, Atmospheric Measurement Techniques, 15, 6201–6219, https://doi.org/10.5194/amt-15-6201-2022, 2022.

Song, A., Li, J., Tsona, N. T., and Du, L.: Parameterizations for sea spray aerosol production flux, Applied Geochemistry, 157, 105776, https://doi.org/10.1016/j.apgeochem.2023.105776, 2023.

Stokes, M. D., Deane, G. B., Prather, K., Bertram, T. H., Ruppel, M. J., Ryder, O. S., Brady, J. M., and Zhao, D.: A Marine Aerosol Reference Tank system as a breaking wave analogue for the production of foam and sea-spray aerosols, Atmospheric Measurement Techniques, 6, 1085–1094, https://doi.org/10.5194/amt-6-1085-2013, 2013.

Von Der Weiden, S. L., Drewnick, F., and Borrmann, S.: Particle Loss Calculator - A new software tool for the assessment of the performance of aerosol inlet systems, Atmospheric Measurement Techniques, 2, 479–494, https://doi.org/10.5194/amt-2-479-2009, 2009.

Williams, A. S., Dedrick, J. L., Russell, L. M., Tornow, F., Silber, I., Fridlind, A. M., Swanson, B., DeMott, P. J., Zieger, P., and Krejci, R.: Aerosol size distribution properties associated with cold-air outbreaks in the Norwegian Arctic, Atmos. Chem. Phys., 24, 11791–11805, https://doi.org/10.5194/acp-24-11791-2024, 2024.

Zábori, J., Matisāns, M., Krejci, R., Nilsson, E. D., and Ström, J.: Artificial primary marine aerosol production: a laboratory study with varying water temperature, salinity, and succinic acid concentration, Atmospheric Chemistry and Physics, 12, 10709–10724, https://doi.org/10.5194/acp-12-10709-2012, 2012.

Zinke, J., Nilsson, E. D., Zieger, P., and Salter, M. E.: The Effect of Seawater Salinity and Seawater Temperature on Sea Salt Aerosol Production, Journal of Geophysical Research: Atmospheres, 127, https://doi.org/10.1029/2021jd036005, 2022.